

Rethinking Disparity: A Depth Range Free Multi-View Stereo Based on Disparity

Qingsong Yan ^{*,1,2}, Qiang Wang ^{*,3}, Kaiyong Zhao ⁴, Bo Li ², Xiaowen Chu ^{†,2,5}, Fei Deng ^{†,1}

¹ Wuhan University, Wuhan, China

² The Hong Kong University of Science and Technology, Hong Kong SAR, China

³ Harbin Institute of Technology (Shenzhen), Shenzhen, China

⁴ XGRIDS, Shenzhen, China

⁵ The Hong Kong University of Science and Technology (Guangzhou), Guangzhou, China

yanqs_wuhu@whu.edu.cn, qiang.wang@hit.edu.cn, kyzhao@xgrids.com, bli@cse.ust.hk
xwchu@ust.hk, fdeng@sgg.whu.edu.cn

Abstract

Existing learning-based multi-view stereo (MVS) methods rely on the depth range to build the 3D cost volume and may fail when the range is too large or unreliable. To address this problem, we propose a disparity-based MVS method based on the epipolar disparity flow (E-flow), called DispMVS, which infers the depth information from the pixel movement between two views. The core of DispMVS is to construct a 2D cost volume on the image plane along the epipolar line between each pair (between the reference image and several source images) for pixel matching and fuse uncountable depths triangulated from each pair by multi-view geometry to ensure multi-view consistency. To be robust, DispMVS starts from a randomly initialized depth map and iteratively refines the depth map with the help of the coarse-to-fine strategy. Experiments on DTUMVS and Tanks&Temple datasets show that DispMVS is not sensitive to the depth range and achieves state-of-the-art results with lower GPU memory.

1 Introduction

Multi-view stereo matching (MVS) is a core technique in 3D reconstruction that has been extensively studied (Gesele et al. 2007; Furukawa and Ponce 2009; Galliani et al. 2015; Schönberger et al. 2016). Although traditional methods try to introduce additional constraints (Xu and Tao 2019; Romanoni and Matteucci 2019; Xu et al. 2020; Wang et al. 2020; Xu and Tao 2020b) to deal with textureless regions or repeated textures, they still have difficulty in guaranteeing the generation of high-quality point clouds in many cases.

Recently, learning-based methods have brought a new light to MVS. MVSNet (Yao et al. 2018) shows a fully differentiable pipeline, which firstly uses a convolutional neural network (CNN) to extract features from input images, and then splits the 3D space into several bins covering a certain depth range to build a 3D cost volume by differentiable homograph, and finally relies on a 3D CNN to regress the depth map. Although MVSNet achieves impressive results on several public benchmarks (Aanaes et al. 2016; Knapitsch et al.

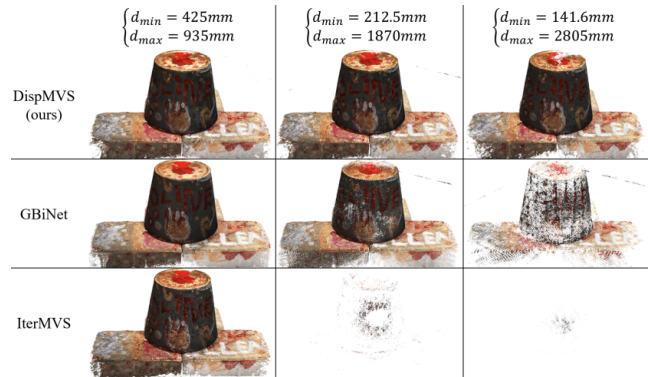


Figure 1: **The influence of the depth range.** This figure compares DispMVS with two state-of-the-art methods (GBiNet (Mi, Di, and Xu 2022) and IterMVS (Wang et al. 2022)) and shows that DispMVS can still generate high-quality point clouds when changing the depth range by Eq. 15. Unlike other methods that use the depth range to build a 3D cost volume and estimate the depth map, DispMVS only builds a 2D cost volume along the epipolar line and uses the multi-view geometry to estimate the depth map.

2017), it is not efficient and requires a lot of GPU memory to infer. Therefore, the coarse-to-fine strategy (Gu et al. 2020; Yang et al. 2020; Cheng et al. 2020; Mi, Di, and Xu 2022) and the recurrent network (Yao et al. 2019; Wei et al. 2021; Wang et al. 2021, 2022) are used to upgrade the MVSNet. The coarse-to-fine strategy uses the coarse stage to recover a coarse depth map and reduces the number of bins needed at the fine stage to reduce the GPU memory. Furthermore, the recurrent network, such as LSTM (Shi et al. 2015) and GRU (Cho et al. 2014), can directly replace the 3D CNN to process the 3D cost volume with a lower GPU memory footprint during the inference. Since these strategies may sacrifice accuracy due to the reduced search range and the lack of global context, many studies have improved the design of loss functions and feature processing modules. In terms of loss functions, there is not only the regression-based method to guide continuous depth (Yao et al. 2018; Gu et al. 2020) but also the classification-based method to guide discrete depth through 3D cost volume (Yao et al. 2019; Mi,

*These authors contributed equally.

†Corresponding author

Di, and Xu 2022), or a mixture of them to achieve better depth prediction quality (Peng et al. 2022). As for the feature processing module, the deformation convolution (Wei et al. 2021), the attention mechanism (Luo et al. 2020), and the Transformer (Zhu et al. 2021) are used to improve the quality of image features. In addition, the visibility information (Xu and Tao 2020c; Zhang et al. 2020) and the epipolar (Ma et al. 2021; Yang et al. 2022) are also used to boost the performance.

A critical issue of those existing methods is the fixed depth range in building the cost volume (Cheng et al. 2020; Mi, Di, and Xu 2022). Usually, the depth range decides the 3D distribution of cost volume that the network attempts to fit, and the size of cost volume is limited to the computational and memory capability, which results in these methods can be easy to over-fit the configured depth range. Fig. 1 shows that the quality of point cloud construction by two state-of-the-art methods, GBiNet (Mi, Di, and Xu 2022) and IterMVS (Wang et al. 2022), is dramatically degraded when the depth range is enlarged. The reason is that these methods cannot capture enough matching information with a fixed number of depth bins.

In this paper, we propose a new MVS pipeline, which allows the CNN to focus only on the matching problem between two different views and relies on the multi-view geometry to recover the depth by matching results. The contributions of this paper are as follows.

- Instead of constructing the 3D cost volume, this paper only constructs the 2D cost volume to match pixels between each pair and generates the depth map by triangulation. In other words, DispMVS exploits the multi-view geometry to reduce the burden of networks, which does not rely on the computationally expensive 3D cost volume to estimate the depth.
- We redesign the flow to deal with the multi-view stereo matching without applying stereo rectification for each pair. First, we propose the epipolar disparity flow (E-flow) and reveal the relationship between the E-flow and the depth. Then we extend E-flow from two-view to multi-view and iteratively update the E-flow by a fused depth to maintain multi-view consistency.
- DispMVS achieves the state-of-the-art result on the DTUMVS and Tanks&Temple without the 3D cost volume, demonstrating the effectiveness of combining multi-view geometry with a learning-based approach.

2 Related Work

With decades of development of MVS, many traditional and learning methods are proposed. Traditional MVS cannot surpass the limitations of the artificially designed matching pipeline and fail to reconstruct the non-Lambertian regions. On the contrary, learning-based methods can automatically find the most helpful information in a data-driven manner, and the benchmarking results of (Aanæs et al. 2016; Knapitsch et al. 2017) show that the learning-based method can easily outperform traditional methods. Generally, the learning-based methods build a 3D cost volume, and we can

categorize them into 3D convolution-based and RNN-based methods according to how they handle the 3D cost volume.

Traditional MVS Traditional MVS has three major types: volumetric method, point cloud method, and depth map method. The volumetric method (Seitz and Dyer 1999; Kutulakos and Seitz 2000; Kostrikov, Horbert, and Leibe 2014) splits the space into inside and outside and cuts out the surface. The point cloud method (Lhuillier and Quan 2005; Goesele et al. 2007; Furukawa and Ponce 2009) reconstructs dense point clouds from sparse point clouds. Although these methods can reconstruct high-quality results, the volumetric and point cloud methods require lots of GPU memory and are hard to parallelize. The depth map method is the most popular, which separately reconstructs the depth map of each view and fuses them to generate the point cloud (Merrell et al. 2007; Galliani et al. 2015). Shen (Shen 2013) and Colmap (Zheng et al. 2014; Schönberger et al. 2016) extends the PatchMatch (Bleyer, Rhemann, and Rother 2011) to multi-view and simultaneously estimates the normal and the depth. Meanwhile, Gipuma (Galliani et al. 2015) and ACMM (Xu and Tao 2019) use a GPU to improve the computational efficiency. The superpixel (Romanoni and Matteucci 2019), the plane (Xu and Tao 2020b), and the mesh (Wang et al. 2020) are used to reduce mismatching in non-Lambertian regions. Although these methods can achieve stable results, they cannot surpass the limitation of hand-craft methods in a challenging environment.

3D Convolution Method Various approaches have been proposed to address the shortcomings of MVSNet (Yao et al. 2018).

The straightforward solution to reduce the GPU memory is building fewer 3D cost volume. Fast-MVSNet (Yu and Gao 2020) only calculates the 3D cost volume on a sparse depth map and propagates the sparse depth map into a dense depth map. CasMVSNet (Gu et al. 2020) and CVP-MVSNet (Yang et al. 2020) uses a coarse-to-fine strategy to deal with the 3D cost volume and reduce computation cost on the high resolution. GBiNet (Mi, Di, and Xu 2022) treats the MVS as a binary search problem and only builds the 3D cost volumes on the side with a high probability of containing the depth.

Various methods are proposed to improve the 3D cost volume quality. P-MVSNet (Luo et al. 2019) uses the isotropic and anisotropic 3D convolution to estimate the depth map. AttMVS (Luo et al. 2020) applies attention mechanism into the 3D cost volume to improve the robustness. UCS-MVSNet (Cheng et al. 2020) uses the uncertainty as a guide to adjust the 3D cost volume. EPP-MVSNet (Ma et al. 2021) propose an epipolar-assembling module to enhance the 3D cost volume. MVSTR (Zhu et al. 2021) relies on the 3D-geometry transformer (Dosovitskiy et al. 2021) to obtain global context and 3D consistency. Also, considering the occlusion, Vis-MVSNet (Zhang et al. 2020) and PVSNet (Xu and Tao 2020c) introduce the visibility to filter out unreliable regions. Besides, MVSCRF (Xue et al. 2019) uses a conditional random field to ensure the smoothness of the depth map, and Uni-MVSNet (Peng et al. 2022) combines the regression and classification by the unified focal loss.

In addition, unsupervised MVS has also achieved impres-

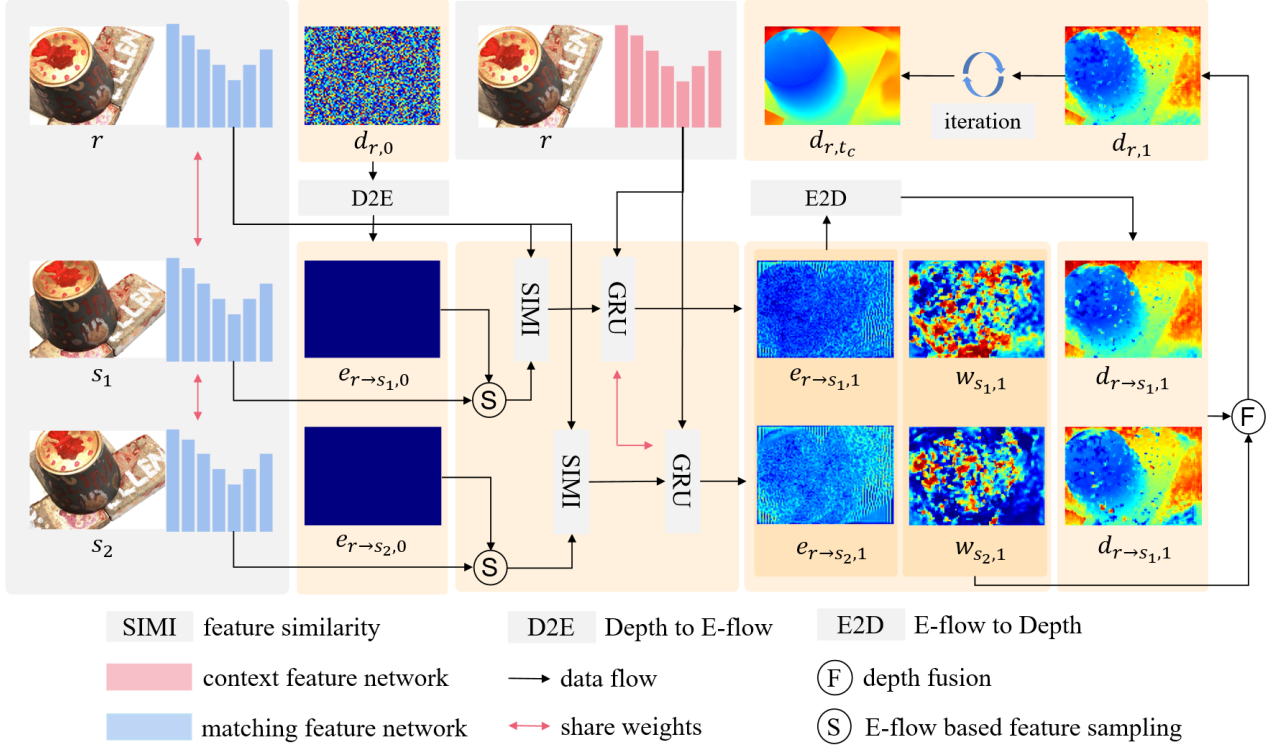


Figure 2: **The pipeline of DispMVS.** After extracting features from input images, DispMVS first uses a random depth map to initialize the E-flow between each pair and then triangulates a new depth map by the E-flow that is updated through a GRU module. Finally, with several iterations, DispMVS can reconstruct a high-quality depth map.

sive results. Un-MVSNet (Khot et al. 2019) uses photometric as a guide to learning the depth map. MVSNet2 (Dai et al. 2019) uses multi-view depth maps to filter out occlusion. M3VSNet (Huang et al. 2021) uses the normal to ensure smoothness and improve the depth map. JADAS (Xu et al. 2021) combines depth and semantics to improve the depth map. RC-MVSNet (Chang et al. 2022) trains a NeRF (Mildenhall et al. 2020) to maintain rendering consistency to solve ambiguity correspondences among views.

RNN Method Instead of using the 3D CNN to process the 3D cost volume, the RNN-based method uses the more efficient LSTM (Shi et al. 2015) or GRU (Cho et al. 2014). R-MVSNet (Yao et al. 2019) uses the GRU to regularize the cost volume sequentially. RED-Net (Liu and Ji 2020) utilizes a 2D recurrent encoder-decoder structure to process the cost volume based on the GRU module. D2HC-RMVSNet (Yan et al. 2020) and AA-RMVSNet (Wei et al. 2021) proposes a hybrid architecture that combines the LSTM and the UNet (Ronneberger, Fischer, and Brox 2015). PatchMatchNet (Wang et al. 2021) introduces an end-to-end PatchMatch (Bleyer, Rhemann, and Rother 2011) with adaptive propagation during each iteration and achieves competitive performance with lower GPU memory. Recently, IterMVS (Wang et al. 2022) uses RAFT (Teed and Deng 2020; Lipson, Teed, and Deng 2021) as backbone and iterative updates the depth map based on the GRU module.

3 Method

In this section, we introduce the details of the proposed method. The pipeline of DispMVS is demonstrated in Fig. 2. Unlike other methods depending on the depth range and differentiable homograph warping to build the 3D cost volume, we use a network to match pixels along the epipolar line and triangulate the depth. Therefore, we first discuss the relationship between the flow, the depth, and the E-flow. Then, we extend the E-flow to multi-view and explain the details of DispMVS and the loss function.

3.1 Flow and Depth

Given a reference view r and a source view s with their interior matrix K_r, K_s and their relative exterior matrix $[R_s, T_s]$, we define d_r, d_s as the depth, and $\vec{f}_{r \rightarrow s}, \vec{f}_{s \rightarrow r}$ as the flow of each view. Assuming that the scene is static, we can convert depth to flow and vice versa according to the multi-view geometry (Hartley and Zisserman 2003).

Depth The depth describes the 3D shape of an image and can re-project a pixel on the image plane to 3D space. Eq. 1 re-projects a pixel p_r in r to P_{p_r} in 3D by its depth $d_r(p_r)$, in which \tilde{p}_r is the homogeneous representation of p_r for computation efficiency. P_{p_r} can also be projected to s by Eq. 2.

$$P_{p_r} = d_r(p_r) K_r^{-1} \tilde{p}_r \quad (1)$$

$$p_s \simeq K_s (R_s P_{p_r} + T_s) \quad (2)$$

Flow The flow describes the movement of pixels on the image plane between two images. For a matched pixel pair p_r in r and p_s in s , we calculate the flow $\vec{f}_{r \rightarrow s}$ by Eq. 3. Generally, the flow does not need to follow geometry constraints and has two degrees of freedom.

$$\vec{f}_{r \rightarrow s}(p_r) = p_s - p_r \quad (3)$$

Depth to Flow Eq. 4 shows how to convert the $d_r(p_r)$ to the $f_r(p_r)$, where \Rightarrow denotes the conversion. We first reproject p_r to P_{p_r} by $d_r(p_r)$ as Eq. 1 shows and then project P_{p_r} to s by Eq. 2 to get the matched pixel p_s . Finally, we can calculate $\vec{f}_{r \rightarrow s}(p_r)$ by Eq. 3.

$$d_r(p_r) \Rightarrow P_{p_r} \Rightarrow p_s \Rightarrow \vec{f}_{r \rightarrow s}(p_r) \quad (4)$$

Flow to Depth Although triangulation is a straightforward method to convert f_r to d_r (Hartley and Zisserman 2003), it has to solve a not differentiable homogeneous linear function. Considering this, we use a differentiable closed-form solution to calculate the depth, even though it is not optimal. Given p_r and $f_{r \rightarrow s}(p_r)$, we can determine p_s by Eq. 3. Based on multi-view geometric consistency, we have the constrain in Eq. 5:

$$d_r(p_r)K_r^{-1}\tilde{p}_r = R_s d_s(p_s)K_s^{-1}\tilde{p}_s + T_s \quad (5)$$

Let $T_s = (t_{sx}, t_{sy}, t_{sz})^T$, $K_r^{-1}\tilde{p}_r = (p_{rx}, p_{ry}, p_{rz})^T$ and $R_s K_s^{-1}\tilde{p}_s = (p_{sx}, p_{sy}, p_{sz})^T$. We can calculate $d_r(p_r)$ by Eq. 6:

$$\begin{cases} d_{xr}(p_r) &= (t_{sx}p_{sz} - t_{sz}p_{rx}) / (p_{sx}p_{sz} - p_{sz}p_{rx}) \\ d_{yr}(p_r) &= (t_{sy}p_{sz} - t_{sz}p_{ry}) / (p_{sy}p_{sz} - p_{sz}p_{ry}) \end{cases} \quad (6)$$

Eq. 6 shows that there are two ways to compute the depth, namely $d_{xr}(p_r)$ and $d_{yr}(p_r)$, since $\vec{f}_{r \rightarrow s}(p_r)$ is a 2D vector that provides flow in x dimension $\vec{f}_{xr \rightarrow xs}(p_r)$ and y dimension $\vec{f}_{yr \rightarrow ys}(p_r)$. Theoretically, $d_{xr}(p_r)$ equals $d_{yr}(p_r)$. However, a smaller flow is not numerically stable and will bring noise into the triangulation. Therefore we select the depth triangulated by the larger flow by Eq. 7:

$$d_r(p_r) = \begin{cases} d_{xr}(p_r) & \text{if } |\vec{f}_{xr \rightarrow xs}(p_r)| \geq |\vec{f}_{yr \rightarrow ys}(p_r)| \\ d_{yr}(p_r) & \text{if } |\vec{f}_{xr \rightarrow xs}(p_r)| < |\vec{f}_{yr \rightarrow ys}(p_r)| \end{cases} \quad (7)$$

3.2 E-flow: the epipolar disparity flow

The flow describes the movement of a pixel on the image plane but does not obey the epipolar geometry, which introduces ambiguity when triangulating the depth. Therefore, we use the epipolar geometry to restrain the flow and define the epipolar disparity flow (E-flow) by Eq. 8, where \vec{e}_{dir} is the normalized direction vector of the epipolar line, and \cdot is the dot product of vectors.

$$e_{r \rightarrow s}(p_r) = \vec{e}_{dir}(p_r) \cdot (p_s - p_r) \quad (8)$$

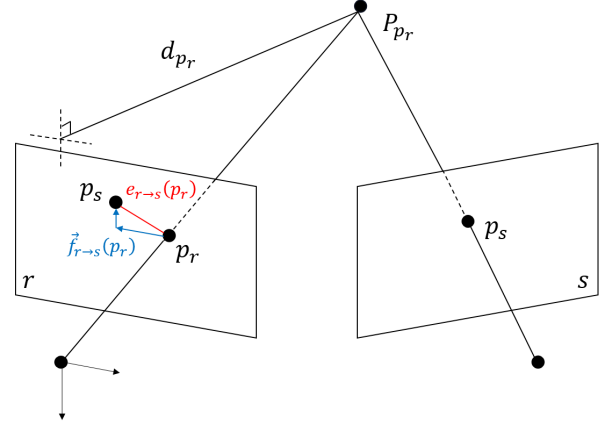


Figure 3: **Depth** (d_{p_r}), **flow** ($\vec{f}_{r \rightarrow s}(p_r)$) and **E-flow** ($e_{r \rightarrow s}(p_r)$). We draw p_s in r to visualize the flow and E-flow. d_{p_r} is the depth of p_r . $\vec{f}_{r \rightarrow s}(p_r)$ and $e_{r \rightarrow s}(p_r)$ describe the way p_r moves. In static scenes, d_{p_r} , $\vec{f}_{r \rightarrow s}(p_r)$ and $e_{r \rightarrow s}(p_r)$ are all correlated and can be converted to each other based on multi-view geometry.

E-flow and Flow Compared with the flow, the E-flow is a scalar and only moves on the epipolar line. In the static scene, the flow and the E-flow are two different ways to describe pixel movement, and their relationship is shown in Eq. 9. Fig. 3 visualizes the flow $\vec{f}_{r \rightarrow s}(p_r)$ and the E-flow $e_{r \rightarrow s}(p_r)$ of pixel p_r .

$$\vec{f}_{r \rightarrow s}(p_r) = \vec{e}_{dir}(p_r) e_{r \rightarrow s}(p_r) \quad (9)$$

E-flow and Depth Considering the relationship between the E-flow and the flow, and the relationship between the flow and the depth, we can convert E-flow to depth, and vice versa by Eq. 10, in which \Leftrightarrow denotes the interconversion.

$$e_{r \rightarrow s} \Leftrightarrow \vec{f}_{r \rightarrow s} \Leftrightarrow d_r \quad (10)$$

3.3 DispMVS

Given a reference image r and N source images s_i ($1 \leq i \leq N$), DispMVS firstly extracts features from all input images and then iteratively updates the depth from random initialization. DispMVS separately estimates the E-flow of each pair by a 2D cost volume and converts the E-flow to the depth for later multi-view depth fusion by a weighted sum. Fig. 2 shows the pipeline of DispMVS with the first iteration at the coarse stage.

Feature Extraction Following RAFT (Teed and Deng 2020), we use two identical encoders to extract features from input images. One encoder simultaneously extracts matching features from input images to calculate similarities. Meanwhile, another encoder extracts context features from the reference image to iteratively update the E-flow. As we apply a coarse-to-fine strategy to speed up efficiency

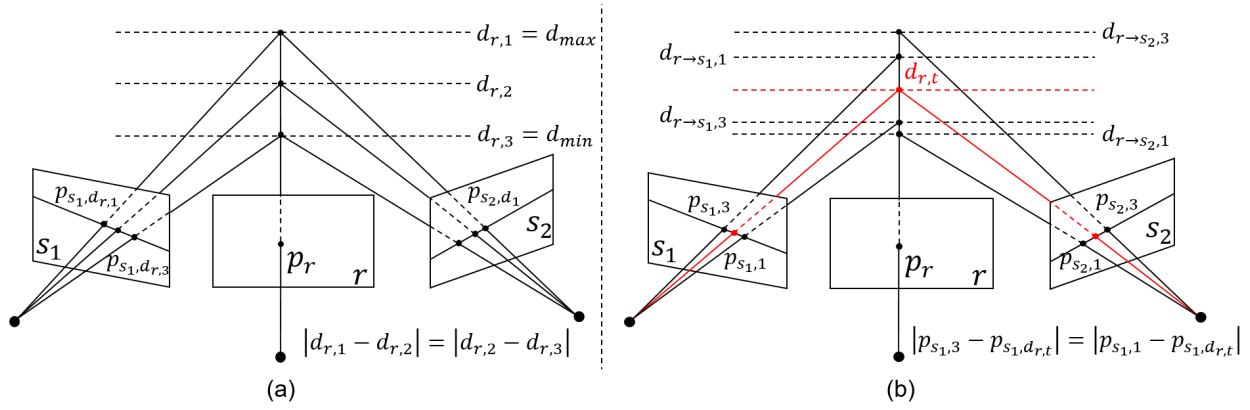


Figure 4: **Different Sampling Spaces.** (a) shows the sampling space of existing methods that evenly samples in the 3D space to build a 3D cost volume. (b) shows the sampling space of DispMVS that evenly samples on each source image plane and estimates the depth by triangulation, whose distribution is decided by the relative poses of the source image.

and accuracy, these encoders use a UNet structure (Ronneberger, Fischer, and Brox 2015) to extract coarse feature maps c_r, c_{s_i} with resolution $1/16$ for the coarse stage and f_r, f_{s_i} with resolution $1/4$ for the fine stage. Besides, we also use the deformable convolutional network (Dai et al. 2017) at the decoder part to capture valuable information.

Initialization of E-flow DispMVS relies on the E-flow to estimate the depth, so it needs an initial depth as the starting point. We adopt the initialization strategy from PatchMatch (Bleyer, Rhemann, and Rother 2011) and initialize $d_{r,0}$ by Eq. 11, where $rand$ comes from a normal distribution, and (d_{min}, d_{max}) are lower and upper bound of the depth range. With $d_{r,0}$, DispMVS can initialize the E-flow for pair by Eq. 10, which is zero for the first iteration. Fig. 2 shows how DispMVS reconstructs a coarse depth from a random depth.

$$\frac{1}{d_{r,0}} = rand \times \left(\frac{1}{d_{min}} - \frac{1}{d_{max}} \right) + \frac{1}{d_{max}} \quad (11)$$

E-flow Estimation After the initialization, DispMVS estimates e_{s_i} of each pair (r, s_i) by the GRU module. For p_r and coarse feature $c_r(p_r)$, DispMVS uses $e_{r \rightarrow s_i}(p_r)$ to find matched point p_{s_i} on s_i and samples feature from $c_{s_i}(p_{s_i})$. To increase the reception field, DispMVS applies m_s times of the average-pool on c_{s_i} to generate features with different scales and evenly samples m_p points around $p_{s_i,t}$ along the epipolar line at each scale with a distance of one pixel. Then, DispMVS calculates the similarity between $c_r(p_r)$ and $m_p \times m_s$ features from c_{s_i} by Eq. 12 to build a 2D cost volume. In the end, DispMVS feeds the cost volume and $e_{r \rightarrow s_i}(p_r)$ to the GRU module to estimate a new $e_{r \rightarrow s_i}(p_r)$ and the weight $w_{s_i}(p_r)$. In DispMVS, we set $m_s = 4$, $m_p = 9$ at the coarse stage and $m_s = 2$, $m_p = 5$ at the fine stage. Fig. 4 compares two different sampling spaces.

$$simi(c_r(p_r), c_{s_i}(p_{s_i})) = \sum_{0 \leq i \leq D} c_r(p_r)[i] c_{s_i}(p_{s_i})[i] \quad (12)$$

Multi-View E-flow Estimation Since the E-flow only applies to two views, DispMVS utilizes a weighted sum to ex-

tend the E-flow to the multi-view situation. DispMVS converts $e_{r \rightarrow s_i}$ to $d_{r \rightarrow s_i}$ by Eq. 10 and then fuses d_r by Eq. 13, where w_{s_i} is normalized by the softmax. To be noted, DispMVS iteratively reconstruct the depth, which means that there are several conversion between the depth and the E-flow, thus further improving multi-view consistency.

$$\begin{cases} w_{s,t+1} = softmax(w_{s,t+1}) \\ d_{r,t+1} = \sum_{1 \leq i \leq N} d_{r \rightarrow s_i, t+1} \times w_{s_i, t+1} \end{cases} \quad (13)$$

Coarse-to-Fine Strategy Following CasMVSNet (Gu et al. 2020), DispMVS uses a coarse-to-fine strategy. DispMVS uses c_r, c_{s_i} with t_c iterations at the coarse stage and f_r, f_{s_i} with t_f iterations at the fine stage. DispMVS starts from a random depth at the coarse stage and upsamples (Teed and Deng 2020) the coarse depth to the fine stage for later refinement. Generally, DispMVS needs more t_c and fewer t_f to improve efficiency and accuracy.

Loss Function As DispMVS outputs a depth in each iteration, we calculate the L1-loss for all depth maps to speed up convergence. To improve the stability of the training procedure, we use the inverse depth range to normalize the ground truth (gt) and the depth $d_{r,i}$. Eq. 14 shows our loss function, in which $\gamma = 0.9$:

$$loss = \sum_{j=t_c, t_f} \sum_{0 \leq i < j} \gamma^i |norm(gt_i) - norm(d_{r,i})| \quad (14)$$

4 Experiments

In this section, we benchmark our DispMVS on two public datasets and compare it with a set of existing methods. We also conduct ablation experiments to explore the effects of different settings of DispMVS.

Datasets We use three different datasets throughout our experiments. The DTUMVS (Aanæs et al. 2016) is an indoor dataset in a controlled environment containing 79 scenes for training, 22 for testing, and 18 for validation. The BlendedMVS (Yao et al. 2020) is a large dataset captured from various outdoor scenes, with 106 scenes for training and the rest

Table 1: **The evaluation results on DTUMVS (Aanæs et al. 2016)**. The lower the Accuracy (Acc), Completeness (Comp), Overall and Mem (GPU Memory), the better. We split methods into three categories and highlight the best in bold for each.

	Method	Acc↓	Comp↓	Overall↓	Mem↓
Trad	Comp (Campbell et al. 2008)	0.835	0.554	0.695	—
	Furu (Furukawa and Ponce 2009)	0.613	0.941	0.777	—
	Tola (Tola, Strelcha, and Fua 2012)	0.342	1.190	0.766	—
	Gipuma (Galliani et al. 2015)	0.283	0.873	0.578	—
Conv	MVSNet (Yao et al. 2018)	0.396	0.527	0.462	9384M
	Point-MVSNet (Chen et al. 2019)	0.342	0.411	0.376	—
	P-MVSNet (Luo et al. 2019)	0.406	0.434	0.420	—
	Fast-MVSNet (Yu and Gao 2020)	0.336	0.403	0.370	—
	CVP-MVSNet (Yang et al. 2020)	0.296	0.406	0.351	—
	Vis-MVSNet (Zhang et al. 2020)	0.369	0.361	0.365	4775M
	CIDER (Xu and Tao 2020a)	0.417	0.437	0.427	—
	CasMVSNet (Gu et al. 2020)	0.325	0.385	0.355	4591M
	UCS-Net (Cheng et al. 2020)	0.338	0.349	0.344	4057M
	EPP-MVSNet (Ma et al. 2021)	0.414	0.297	0.355	—
	UniMVSNet (Peng et al. 2022)	0.352	0.278	0.315	3216M
GBiNet (Mi, Di, and Xu 2022)	0.315	0.262	0.289	2018M	
RNN	R-MVSNet (Yao et al. 2019)	0.383	0.452	0.417	—
	D2HC-RMVSNet (Yan et al. 2020)	0.395	0.378	0.386	—
	AA-RMVSNet (Wei et al. 2021)	0.376	0.339	0.357	11973M
	PatchMatchNet (Wang et al. 2021)	0.427	0.277	0.352	1629M
	IterMVS (Wang et al. 2022)	0.373	0.354	0.363	842M
	DispMVS (ours)	0.354	0.324	0.339	1368M



Figure 5: **Point clouds** We visualize some point clouds generated by DispMVS on DTUMVS (Aanæs et al. 2016) and Tanks & Temple (Knapitsch et al. 2017).

7 scenes for testing. The Tanks&Temple (Knapitsch et al. 2017) is an outdoor multi-view stereo benchmark that contains 14 real-world scenes under complex conditions.

Implementation We implement DispMVS by PyTorch (Paszke et al. 2019) and train two models on the DTUMVS and the BlendedMVS separately. On the DTUMVS, we set the image resolution to 640×512 and $N = 5$. On the BlendedMVS, we set the image resolution to 768×576 and $N = 5$. For all models, we apply the training strategy in PatchmatchNet (Wang et al. 2021) for better learning of the weight and use the Adam (Kingma and Ba 2015) ($\beta_1 = 0.9, \beta_2 = 0.999$) optimizer with an initial learning rate of 0.0002 that halves every four epochs for 16 epochs. The training procedure is finished on two V100 with $t_c = 8, t_f = 2$ considering the GPU memory limitation. During the evaluation, we filter and fuse all depth maps into point clouds to compare with the ground truth.

4.1 Evaluation on DTUMVS

We evaluate the DTUMVS on the test part and resize all images to 1600×1152 with $N = 5$. Table 1 compares Disp-

MVS with other state-of-the-art methods. We split existing methods into traditional methods, 3D convolution-based methods, and RNN-based methods. DispMVS has the best overall score among RNN-based methods and is 0.024 lower than IterMVS (Wang et al. 2022) and 0.018 lower than AA-RMVSNet (Wei et al. 2021). DispMVS ranks the 3rd among all methods. GBiNet (Mi, Di, and Xu 2022) and UniMVS-Net (Peng et al. 2022) are the top two methods, but they incur much higher GPU memory. We visualize some point clouds of DTUMVS generated by DispMVS in the first row of Fig. 5. These qualitative and quantitative experimental results demonstrate the effectiveness of DispMVS in obtaining depth by triangulation, even though DispMVS does not construct any 3D cost volume.

4.2 Evaluation on Tanks&Temple

As Tanks&Temple does not provide training samples, we apply the model pretrained on the BlendedMVS to it. We resize all images of Tanks&Temple to 1600×1152 and set $N = 7$. Table 2 shows the results of learning-based methods, split into 3D convolution-based and RNN-based. Tanks&Temple contains two subsets, Intermedia and Advanced. DispMVS achieves the best mean score on the Advanced subset among the RNN-based method. Although AA-RMVSNet (Wei et al. 2021) outperforms DispMVS on the Intermedia subset, AA-RMVSNet uses nearly ten times more GPU memory than DispMVS. Overall, the results on Tanks&Temple demonstrate that DispMVS has robust generalization with a low amount of GPU memory. The second row of Fig. 5 shows point clouds generated on the Tanks&Temple by DispMVS.

4.3 Ablation Studies

In this subsection, we discuss the core parts of our method. Considering that the RAFT structure has been thoroughly studied in (Teed and Deng 2020; Lipson, Teed, and Deng 2021; Wang et al. 2022), we conduct ablation experiments on the coarse-to-fine strategy, the random initialization, and the changes in depth range. Throughout all ablation experiments, we use the DTUMVS as a baseline dataset.

The coarse-to-fine strategy DispMVS-M firstly estimates the depth with the feature from $1/16$ and refines the depth with the feature from $1/4$. DispMVS-S only extracts features from $1/8$ to recover the depth map to make the comparison fairer. Table. 3 shows that the coarse-to-fine strategy dramatically improves the overall score from 0.455 for DispMVS-M to 0.339 for DispMVS-S. Therefore, we choose DispMVS-M as the method used in this paper.

Random Initialization Unlike existing methods that build the 3D cost volume from a known depth range, DispMVS starts from a random initial depth, which means that the input of DispMVS could be different every time. To measure the effects of the random initialization, we conduct three times of initialization without fixing the random seed and evaluate point clouds. Table 4 shows that the variance of metrics between different inferences is smaller than $1e-6$, which proves that DispMVS are robust to the random initial depth and can always generate a high-quality depth map.

Table 2: **The evaluation results on Tanks & Temple (Knapitsch et al. 2017)**. Higher scores indicate higher quality of the point cloud. We split methods into two categories and highlight the best in bold for each.

Method	Advanced							Intermediate								
	Mean	Aud.	Bal.	Cou.	Mus.	Pal.	Tem.	Mean	Fam.	Fra.	Hor.	Lig.	M60	Pan.	Pla.	Tra
MVSNet (Yao et al. 2018)	-	-	-	-	-	-	-	43.48	55.99	28.55	25.07	50.79	53.96	50.86	47.90	34.69
Point-MVSNet (Chen et al. 2019)	-	-	-	-	-	-	-	48.27	61.79	41.15	34.20	50.79	51.97	50.85	52.38	43.06
UCS-Net (Cheng et al. 2020)	-	-	-	-	-	-	-	54.83	76.09	53.16	43.03	54.00	55.60	51.49	57.38	47.89
Vis-MVSNet (Zhang et al. 2020)	33.78	20.79	38.77	32.45	44.20	28.73	37.70	60.03	77.40	60.23	47.07	63.44	62.21	57.28	60.54	52.07
CasMVSNet (Gu et al. 2020)	31.12	19.81	38.46	29.10	43.87	27.36	28.11	56.42	76.36	58.45	46.20	55.53	56.11	54.02	58.17	46.56
EPP-MVSNet (Ma et al. 2021)	35.72	21.28	39.74	35.34	49.21	30.00	38.75	61.68	77.86	60.54	52.96	62.33	61.69	60.34	62.44	55.30
UniMVSNet (Peng et al. 2022)	38.96	28.33	44.36	39.74	52.89	33.80	34.63	64.36	81.20	66.43	53.11	63.46	66.09	64.84	62.23	57.53
GBiNet (Mi, Di, and Xu 2022)	37.32	29.77	42.12	36.30	47.69	31.11	36.93	61.42	79.77	67.69	51.81	61.25	60.37	55.87	60.67	53.89
R-MVSNet (Yao et al. 2019)	24.91	12.55	29.09	25.06	38.68	19.14	24.96	48.40	69.96	46.65	32.59	42.95	51.88	48.80	52.00	42.38
D2HC-RMVSNet (Yan et al. 2020)	-	-	-	-	-	-	-	59.20	74.69	56.04	49.42	60.08	59.81	59.61	60.04	53.92
AA-RMVSNet (Wei et al. 2021)	33.53	20.96	40.15	32.05	46.01	29.28	32.71	61.51	77.77	59.53	51.53	64.02	64.05	59.47	60.85	54.90
PatchmatchNet (Wang et al. 2021)	32.31	23.69	37.73	30.04	41.80	28.31	32.29	53.15	66.99	52.64	43.24	54.87	52.87	49.54	54.21	50.81
IterMVS (Wang et al. 2022)	33.24	22.95	38.74	30.64	43.44	28.39	35.27	56.94	76.12	55.80	50.53	56.05	57.68	52.62	55.70	50.99
DispMVS (ours)	34.90	26.09	38.01	33.19	44.90	28.49	38.75	59.07	74.73	60.67	54.13	59.58	58.02	53.39	58.63	53.42

Table 3: **Comparison between single stage and multi stage**. “-S” indicates reconstruction with only one resolution at 1/8, while “-M” indicates reconstruction with multiple resolutions (the method in this paper).

Method	Acc↓	Comp↓	Overall↓
DispMVS-S	0.500	0.410	0.455
DispMVS-M	0.354	0.324	0.339

Depth Range The existing MVS methods split a given depth range into several bins and build a 3D cost volume by differentiable homography. However, DispMVS is insensitive to the depth range as it only constructs a 2D cost volume on the image plane along the epipolar line. We select two state-of-the-art methods (GBiNet (Mi, Di, and Xu 2022) and IterMVS (Wang et al. 2022)) and manually change the depth range by Eq. 15. All methods are trained by the same dataset with the same depth range. Table. 5 shows that performance of GBiNet and IterMVS decreases dramatically, but DispMVS can be robust to these changes. Fig. 1 visualizes point clouds generated by different methods with different depth ranges, where GBiNet and IterMVS cannot converge when the depth range is too large.

$$range_x = \begin{cases} d_{min} & = d_{min}/x \\ d_{max} & = d_{max} \times x \end{cases} \quad (15)$$

4.4 Limitations

As DispMVS needs to keep building the 2D cost volume during the iteration, its computational efficiency is relatively low. In our experiment, DispMVS needs around 0.7 seconds to process a view on the DTUMVS. Compared with IterMVS (Wang et al. 2022) which only needs around 0.3 seconds per view, DispMVS needs a more efficient epipolar matching module. In addition, DispMVS needs around 48G GPU memory during training because DispMVS needs several iterations to update the depth by the GRU module, which needs to save all gradients and intermediate results.

Table 4: **Evaluate the random initialization**. A lower variance means the difference between multi results is smaller.

Method	Acc↓	Comp↓	Overall↓
rand-1	0.353829	0.324110	0.338970
rand-2	0.354811	0.324946	0.339878
rand-3	0.354272	0.324324	0.339298
variance	2.418e-7	1.890e-7	2.110e-7

Table 5: **Influences of changing the depth range**. The lower, the better for all metrics under different depth ranges.

Range	Method	Acc↓	Comp↓	Overall↓
$range_1$	GBiNet (Mi, Di, and Xu 2022)	0.315	0.262	0.289
	IterMVS (Wang et al. 2022)	0.373	0.354	0.363
	DispMVS (ours)	0.354	0.324	0.339
$range_2$	GBiNet (Mi, Di, and Xu 2022)	0.480	0.556	0.518
	IterMVS (Wang et al. 2022)	0.532	1.471	1.002
	DispMVS (ours)	0.348	0.404	0.376
$range_3$	GBiNet (Mi, Di, and Xu 2022)	0.618	1.303	0.960
	IterMVS (Wang et al. 2022)	0.935	6.985	3.960
	DispMVS (ours)	0.314	0.671	0.493

5 Conclusion

This paper introduces a new pipeline of MVS, called DispMVS, which does not need to build any 3D cost volumes but triangulates the depth map by multi-view geometry. DispMVS is a depth range invariant method and can be generalized to the dataset with different ranges with the training set, which proves that 3D cost volume is unnecessary for MVS. Compared with existing learning-based methods, DispMVS lets the network focus on matching pixels that the CNN network is good at and uses the multi-view geometry to deal with the geometry information. Experiments on datasets show that DispMVS achieves comparable results with other 3D convolution methods and outperforms RNN-based methods with a lower GPU memory requirement.

Acknowledgments This work was supported in part by grant RMGS2021-8-10 from Hong Kong Research Matching Grant Scheme and the NVIDIA Academic Hardware Grant.

Supplementary material

1 Depth Normalization

To make our method more numeric stable, we apply a depth normalization by Eq. 16, where we use the inversed minimum depth d_{min} and inversed maximum depth d_{max} to normalize the input depth. The depth normalization can decrease the effect of outliers, especially in the multi-view depth fusion and the loss function. In the multi-view depth fusion, we convert the epipolar disparity flow (E-flow) to depth by triangulation, which may introduce outliers when E-flow is too small. As for the loss function, the normalization can make it easier for the network to converge when the depth range is different among datasets.

$$depth_norm = \frac{1/depth - 1/depth_{max}}{1/depth_{min} - 1/depth_{max}} \quad (16)$$

2 GRU Update

To update the E-flow, we utilize two GRU modules at the coarse and fine stages of DispMVS with the same network structure of RAFT (Teed and Deng 2020). The input and output of this module is seen in Eq. 17, where f_t, f_r, f_h are 2D convolution networks and W_t, W_r, W_h are the corresponding parameters. After updating E-flow, we triangulate the depth and fuse them in each iteration. Fig. 6 shows the depth maps generated by DispMVS on DTU and Tanks&Temple, in which we can see that the depth map recovers from coarse to fine.

$$\begin{cases} z_t &= \sigma(f_t([h_{t-1}, x_t], W_t)) \\ r_t &= \sigma(f_r([h_{t-1}, x_t], W_r)) \\ \tilde{h}_t &= \tanh(f_h([r_t \odot h_{t-1}, x_t], W_h)) \\ h_t &= (1 - z_t) \odot h_{t-1} + z_t \odot \tilde{h}_t \end{cases} \quad (17)$$

3 Depth Upsampling

Following RAFT (Teed and Deng 2020), we upsample a coarse depth map to a fine depth map through a convex combination of each pixel’s nine neighbors instead of directly using the bilinear upsampling. Since this upsampling module acquires the fusion weights by learning, it can retain more details and have sharp edges at the boundaries.

4 Depth Fusion

DispMVS only predicts the depth map and needs to fuse them to point clouds for further evaluation. The fusion can filter the depth map to remove inconsistent regions and reduce the noise in the point cloud. Following MVSNet (Yao et al. 2018), we use geometric consistency to filter out inconsistent regions and reduce the noise in the point cloud. Geometric consistency contains two steps, the first step projects depth maps of source images to the reference image to mask out regions with large depth differences, and the second step reprojects the depth map of the reference image to source images to mask out regions with large pixel

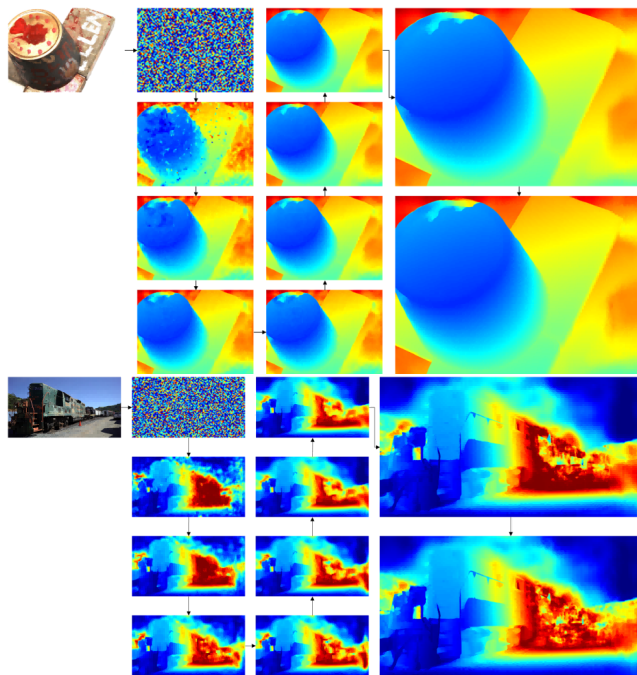


Figure 6: **Depth Maps in each iteration on DTUMVS and Tanks&Temple** DispMVS iteratively recovers the depth map. An interesting phenomenon is that DispMVS cannot reconstruct the sky region, where DispMVS cannot find reliable matches and is far away from the view. But DispMVS can reconstruct the thin structure nearby.

displacements. Besides, DispMVS also uses the depth range to filter out points out of bound. After filtering out these inconsistent regions and invalid regions, DispMVS reproject pixels to 3D space to generate point clouds. Fig. 7 and Fig. 8 show point clouds generated by DispMVS.

References

- Aanæs, H.; Jensen, R. R.; Vogiatzis, G.; Tola, E.; and Dahl, A. B. 2016. Large-scale data for multiple-view stereopsis. *International Journal of Computer Vision*, 120(2): 153–168.
- Bleyer, M.; Rhemann, C.; and Rother, C. 2011. Patchmatch stereo-stereo matching with slanted support windows. In *Bmvc*, volume 11, 1–11.
- Campbell, N. D.; Vogiatzis, G.; Hernández, C.; and Cipolla, R. 2008. Using multiple hypotheses to improve depth-maps for multi-view stereo. In *European Conference on Computer Vision*, 766–779. Springer.
- Chang, D.; Božič, A.; Zhang, T.; Yan, Q.; Chen, Y.; Süssstrunk, S.; and Nießner, M. 2022. RC-MVSNet: Unsupervised Multi-View Stereo with Neural Rendering. In *European conference on computer vision*.
- Chen, R.; Han, S.; Xu, J.; and Su, H. 2019. Point-based multi-view stereo network. In *Proceedings of the IEEE/CVF international conference on computer vision*, 1538–1547.
- Cheng, S.; Xu, Z.; Zhu, S.; Li, Z.; Li, L. E.; Ramamoorthi, R.; and Su, H. 2020. Deep stereo using adaptive thin volume

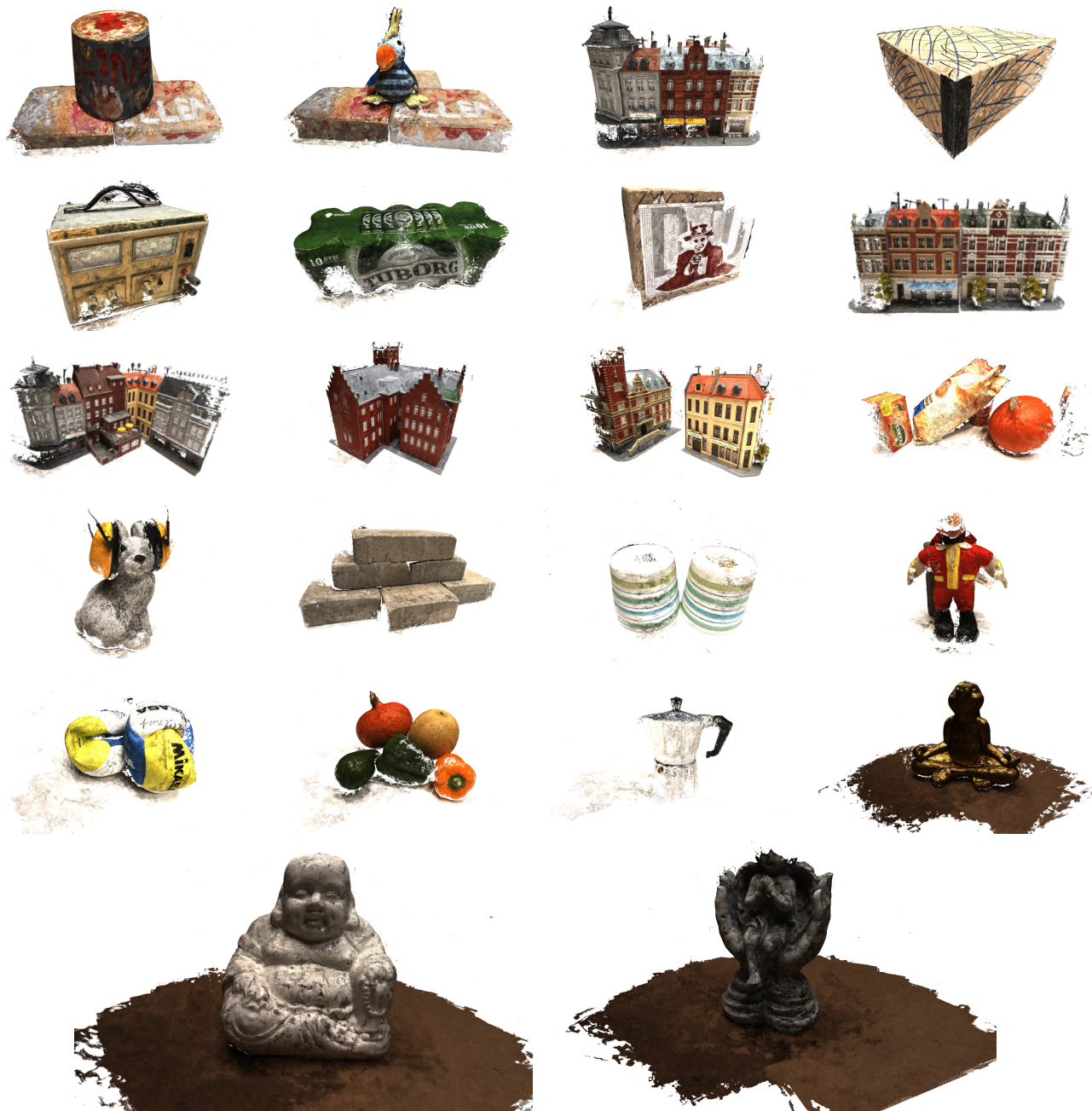


Figure 7: Results on DTUMVS We visualize 22 scenes in the test.

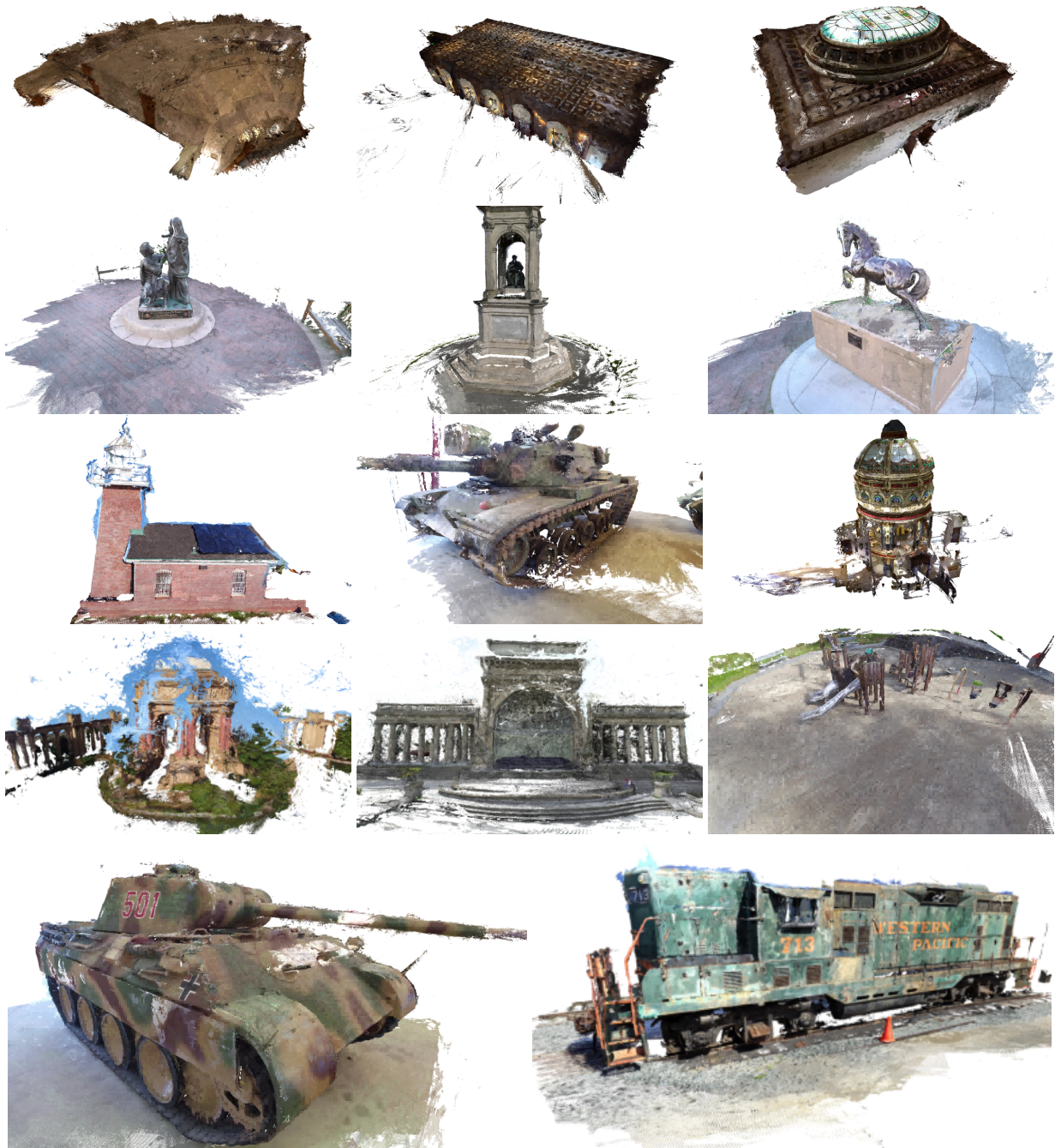


Figure 8: Results on Tanks&Temple We visualize all scenes in Intermedia and Advanced.

- representation with uncertainty awareness. In *Proceedings of the IEEE/CVF Conference on Computer Vision and Pattern Recognition*, 2524–2534.
- Cho, K.; Van Merriënboer, B.; Gulcehre, C.; Bahdanau, D.; Bougares, F.; Schwenk, H.; and Bengio, Y. 2014. Learning phrase representations using RNN encoder-decoder for statistical machine translation. In *Proceedings of the 2014 Conference on Empirical Methods in Natural Language Processing*, 1724–1734.
- Dai, J.; Qi, H.; Xiong, Y.; Li, Y.; Zhang, G.; Hu, H.; and Wei, Y. 2017. Deformable convolutional networks. In *Proceedings of the IEEE international conference on computer vision*, 764–773.
- Dai, Y.; Zhu, Z.; Rao, Z.; and Li, B. 2019. Mvs2: Deep unsupervised multi-view stereo with multi-view symmetry. In *2019 International Conference on 3D Vision (3DV)*, 1–8. Ieee.
- Dosovitskiy, A.; Beyer, L.; Kolesnikov, A.; Weissenborn, D.; Zhai, X.; Unterthiner, T.; Dehghani, M.; Minderer, M.; Heigold, G.; Gelly, S.; et al. 2021. An image is worth 16x16 words: Transformers for image recognition at scale. In *International Conference on Learning Representations*.
- Furukawa, Y.; and Ponce, J. 2009. Accurate, dense, and robust multiview stereopsis. *IEEE transactions on pattern analysis and machine intelligence*, 32(8): 1362–1376.
- Galliani, S.; et al. 2015. Massively parallel multiview stereopsis by surface normal diffusion. In *Proceedings of the IEEE International Conference on Computer Vision*, 873–881.
- Goesele, M.; Snavely, N.; Curless, B.; Hoppe, H.; and Seitz, S. M. 2007. Multi-view stereo for community photo collections. In *2007 IEEE 11th International Conference on Computer Vision*, 1–8. IEEE.
- Gu, X.; Fan, Z.; Zhu, S.; Dai, Z.; Tan, F.; and Tan, P. 2020. Cascade cost volume for high-resolution multi-view stereo and stereo matching. In *Proceedings of the IEEE/CVF Conference on Computer Vision and Pattern Recognition*, 2495–2504.
- Hartley, R.; and Zisserman, A. 2003. *Multiple view geometry in computer vision*. Cambridge university press.
- Huang, B.; Yi, H.; Huang, C.; He, Y.; Liu, J.; and Liu, X. 2021. M3VSNet: Unsupervised multi-metric multi-view stereo network. In *2021 IEEE International Conference on Image Processing (ICIP)*, 3163–3167. IEEE.
- Khot, T.; Agrawal, S.; Tulsiani, S.; Mertz, C.; Lucey, S.; and Hebert, M. 2019. Learning unsupervised multi-view stereopsis via robust photometric consistency. *arXiv preprint arXiv:1905.02706*.
- Kingma, D. P.; and Ba, J. 2015. Adam: A Method for Stochastic Optimization. In *International Conference on Learning Representations*.
- Knapitsch, A.; Park, J.; Zhou, Q.-Y.; and Koltun, V. 2017. Tanks and temples: Benchmarking large-scale scene reconstruction. *ACM Transactions on Graphics (ToG)*, 36(4): 1–13.
- Kostrikov, I.; Horbert, E.; and Leibe, B. 2014. Probabilistic labeling cost for high-accuracy multi-view reconstruction. In *Proceedings of the IEEE conference on computer vision and pattern recognition*, 1534–1541.
- Kutulakos, K. N.; and Seitz, S. M. 2000. A theory of shape by space carving. *International journal of computer vision*, 38: 199–218.
- Lhuillier, M.; and Quan, L. 2005. A quasi-dense approach to surface reconstruction from uncalibrated images. *IEEE transactions on pattern analysis and machine intelligence*, 27: 418–433.
- Lipson, L.; Teed, Z.; and Deng, J. 2021. Raft-stereo: Multilevel recurrent field transforms for stereo matching. In *2021 International Conference on 3D Vision (3DV)*, 218–227. IEEE.
- Liu, J.; and Ji, S. 2020. A novel recurrent encoder-decoder structure for large-scale multi-view stereo reconstruction from an open aerial dataset. In *Proceedings of the IEEE/CVF conference on computer vision and pattern recognition*, 6050–6059.
- Luo, K.; Guan, T.; Ju, L.; Huang, H.; and Luo, Y. 2019. P-mvsnet: Learning patch-wise matching confidence aggregation for multi-view stereo. In *Proceedings of the IEEE/CVF International Conference on Computer Vision*, 10452–10461.
- Luo, K.; Guan, T.; Ju, L.; Wang, Y.; Chen, Z.; and Luo, Y. 2020. Attention-aware multi-view stereo. In *Proceedings of the IEEE/CVF Conference on Computer Vision and Pattern Recognition*, 1590–1599.
- Ma, X.; Gong, Y.; Wang, Q.; Huang, J.; Chen, L.; and Yu, F. 2021. EPP-MVSNet: Epipolar-assembling based Depth Prediction for Multi-view Stereo. In *Proceedings of the IEEE/CVF International Conference on Computer Vision*, 5732–5740.
- Merrell, P.; Akbarzadeh, A.; Wang, L.; Mordohai, P.; Frahm, J.-M.; Yang, R.; Nistér, D.; and Pollefeys, M. 2007. Real-time visibility-based fusion of depth maps. In *2007 IEEE 11th International Conference on Computer Vision*, 1–8. Ieee.
- Mi, Z.; Di, C.; and Xu, D. 2022. Generalized Binary Search Network for Highly-Efficient Multi-View Stereo. In *Proceedings of the IEEE/CVF Conference on Computer Vision and Pattern Recognition*, 12991–13000.
- Mildenhall, B.; Srinivasan, P. P.; Tancik, M.; Barron, J. T.; Ramamoorthi, R.; and Ng, R. 2020. Nerf: Representing scenes as neural radiance fields for view synthesis. In *European conference on computer vision*, 405–421. Springer.
- Paszke, A.; Gross, S.; Massa, F.; Lerer, A.; Bradbury, J.; Chanan, G.; Killeen, T.; Lin, Z.; Gimelshein, N.; Antiga, L.; et al. 2019. Pytorch: An imperative style, high-performance deep learning library. *Advances in neural information processing systems*, 32.
- Peng, R.; Wang, R.; Wang, Z.; Lai, Y.; and Wang, R. 2022. Rethinking Depth Estimation for Multi-View Stereo: A Unified Representation. In *Proceedings of the IEEE/CVF Conference on Computer Vision and Pattern Recognition*, 8645–8654.

- Romanoni, A.; and Matteucci, M. 2019. Tapa-mvs: Textureless-aware patchmatch multi-view stereo. In *Proceedings of the IEEE/CVF International Conference on Computer Vision*, 10413–10422.
- Ronneberger, O.; Fischer, P.; and Brox, T. 2015. U-net: Convolutional networks for biomedical image segmentation. In *International Conference on Medical image computing and computer-assisted intervention*, 234–241. Springer.
- Schönberger, J. L.; Zheng, E.; Frahm, J.-M.; and Pollefeys, M. 2016. Pixelwise view selection for unstructured multi-view stereo. In *European conference on computer vision*, 501–518. Springer.
- Seitz, S. M.; and Dyer, C. R. 1999. Photorealistic scene reconstruction by voxel coloring. *International Journal of Computer Vision*, 35: 151–173.
- Shen, S. 2013. Accurate multiple view 3d reconstruction using patch-based stereo for large-scale scenes. *IEEE transactions on image processing*, 22(5): 1901–1914.
- Shi, X.; Chen, Z.; Wang, H.; Yeung, D.-Y.; Wong, W.-K.; and Woo, W.-c. 2015. Convolutional LSTM network: A machine learning approach for precipitation nowcasting. *Advances in neural information processing systems*, 28.
- Teed, Z.; and Deng, J. 2020. Raft: Recurrent all-pairs field transforms for optical flow. In *European conference on computer vision*, 402–419. Springer.
- Tola, E.; Strecha, C.; and Fua, P. 2012. Efficient large-scale multi-view stereo for ultra high-resolution image sets. *Machine Vision and Applications*, 23(5): 903–920.
- Wang, F.; Galliani, S.; Vogel, C.; Speciale, P.; and Pollefeys, M. 2021. Patchmatchnet: Learned multi-view patchmatch stereo. In *Proceedings of the IEEE/CVF Conference on Computer Vision and Pattern Recognition*, 14194–14203.
- Wang, F.; et al. 2022. IterMVS: Iterative Probability Estimation for Efficient Multi-View Stereo. In *Proceedings of the IEEE/CVF Conference on Computer Vision and Pattern Recognition*, 8606–8615.
- Wang, Y.; Guan, T.; Chen, Z.; Luo, Y.; Luo, K.; and Ju, L. 2020. Mesh-guided multi-view stereo with pyramid architecture. In *Proceedings of the IEEE/CVF Conference on Computer Vision and Pattern Recognition*, 2039–2048.
- Wei, Z.; Zhu, Q.; Min, C.; Chen, Y.; and Wang, G. 2021. Aarmvsnet: Adaptive aggregation recurrent multi-view stereo network. In *Proceedings of the IEEE/CVF International Conference on Computer Vision*, 6187–6196.
- Xu, H.; Zhou, Z.; Qiao, Y.; Kang, W.; and Wu, Q. 2021. Self-supervised multi-view stereo via effective co-segmentation and data-augmentation. In *Proceedings of the AAAI Conference on Artificial Intelligence*, volume 35, 3030–3038.
- Xu, Q.; and Tao, W. 2019. Multi-scale geometric consistency guided multi-view stereo. In *Proceedings of the IEEE/CVF Conference on Computer Vision and Pattern Recognition*, 5483–5492.
- Xu, Q.; and Tao, W. 2020a. Learning inverse depth regression for multi-view stereo with correlation cost volume. In *Proceedings of the AAAI Conference on Artificial Intelligence*, volume 34, 12508–12515.
- Xu, Q.; and Tao, W. 2020b. Planar prior assisted patchmatch multi-view stereo. In *Proceedings of the AAAI Conference on Artificial Intelligence*, volume 34, 12516–12523.
- Xu, Q.; and Tao, W. 2020c. Pvsnet: Pixelwise visibility-aware multi-view stereo network. *arXiv preprint arXiv:2007.07714*.
- Xu, Z.; Liu, Y.; Shi, X.; Wang, Y.; and Zheng, Y. 2020. Mar-mvs: Matching ambiguity reduced multiple view stereo for efficient large scale scene reconstruction. In *Proceedings of the IEEE/CVF Conference on Computer Vision and Pattern Recognition*, 5981–5990.
- Xue, Y.; Chen, J.; Wan, W.; Huang, Y.; Yu, C.; Li, T.; and Bao, J. 2019. Mvsrfr: Learning multi-view stereo with conditional random fields. In *Proceedings of the IEEE/CVF International Conference on Computer Vision*, 4312–4321.
- Yan, J.; Wei, Z.; Yi, H.; Ding, M.; Zhang, R.; Chen, Y.; Wang, G.; and Tai, Y.-W. 2020. Dense hybrid recurrent multi-view stereo net with dynamic consistency checking. In *European conference on computer vision*, 674–689. Springer.
- Yang, J.; Mao, W.; Alvarez, J. M.; and Liu, M. 2020. Cost volume pyramid based depth inference for multi-view stereo. In *Proceedings of the IEEE/CVF Conference on Computer Vision and Pattern Recognition*, 4877–4886.
- Yang, Z.; Ren, Z.; Shan, Q.; and Huang, Q. 2022. Mvs2d: Efficient multi-view stereo via attention-driven 2d convolutions. In *Proceedings of the IEEE/CVF Conference on Computer Vision and Pattern Recognition*, 8574–8584.
- Yao, Y.; Luo, Z.; Li, S.; Fang, T.; and Quan, L. 2018. Mvsnet: Depth inference for unstructured multi-view stereo. In *Proceedings of the European conference on computer vision (ECCV)*, 767–783.
- Yao, Y.; Luo, Z.; Li, S.; Shen, T.; Fang, T.; and Quan, L. 2019. Recurrent mvsnet for high-resolution multi-view stereo depth inference. In *Proceedings of the IEEE/CVF conference on computer vision and pattern recognition*, 5525–5534.
- Yao, Y.; Luo, Z.; Li, S.; Zhang, J.; Ren, Y.; Zhou, L.; Fang, T.; and Quan, L. 2020. Blendedmvs: A large-scale dataset for generalized multi-view stereo networks. In *Proceedings of the IEEE/CVF Conference on Computer Vision and Pattern Recognition*, 1790–1799.
- Yu, Z.; and Gao, S. 2020. Fast-mvsnet: Sparse-to-dense multi-view stereo with learned propagation and gauss-newton refinement. In *Proceedings of the IEEE/CVF Conference on Computer Vision and Pattern Recognition*, 1949–1958.
- Zhang, J.; Yao, Y.; Li, S.; Luo, Z.; and Fang, T. 2020. Visibility-aware Multi-view Stereo Network. In *British Machine Vision Conference*.
- Zheng, E.; Dunn, E.; Jovic, V.; and Frahm, J.-M. 2014. Patchmatch based joint view selection and depthmap estimation. In *Proceedings of the IEEE Conference on Computer Vision and Pattern Recognition*, 1510–1517.
- Zhu, J.; Peng, B.; Li, W.; Shen, H.; Zhang, Z.; and Lei, J. 2021. Multi-View Stereo with Transformer. *arXiv preprint arXiv:2112.00336*.